


Detecting the Néel vector of altermagnets in heterostructures with a topological insulator and a crystalline valley-edge insulator

Motohiko Ezawa 

Department of Applied Physics, The University of Tokyo, 7-3-1 Hongo, Tokyo 113-8656, Japan



(Received 14 March 2024; revised 7 May 2024; accepted 11 June 2024; published 24 June 2024)

We investigate topological phases in a bilayer system composed of an altermagnet and a two-dimensional topological insulator described by the Bernevig-Hughes-Zhang model. A topological phase transition occurs from a first-order topological insulator to a trivial insulator at a certain critical altermagnetization if the Néel vector of altermagnet is along the x or y axis. It is intriguing that valley-protected edge states emerge along the Néel vector in this trivial insulator, which are as stable as the topological edge states. We name it a crystalline valley-edge insulator. On the other hand, the system turns out to be a second-order topological insulator when the Néel vector is along the z axis. The tunneling conductance has a strong dependence on the Néel vector. In addition, the band gap depends on the Néel vector, which is measurable by optical absorption. Hence, it is possible experimentally to detect the Néel vector by measuring tunneling conductance and optical absorption.

DOI: [10.1103/PhysRevB.109.245306](https://doi.org/10.1103/PhysRevB.109.245306)

I. INTRODUCTION

Recently, altermagnets have attracted rapid growth of interest [1–3]. Altermagnets are promising candidates for future spintronics [1–3]. Ultra-high-density memories with ultrahigh flip rate may be realized owing to the zero net magnetization. It is difficult to detect the direction of the Néel vector due to the zero net magnetization in general [4–10]. Nevertheless, the z component of the Néel vector can be read out via anomalous Hall effect in altermagnets [11–14].

An altermagnet is the third-type of magnets in terms of symmetry [1–3]. Altermagnets have a combinational symmetry of time-reversal symmetry and rotational symmetry. Especially, d -wave altermagnet has a combination symmetry of time-reversal symmetry and four-fold rotational symmetry. On the other hand, ferromagnets break time-reversal symmetry, while antiferromagnets has a combinational symmetry of time-reversal symmetry and one-site translational symmetry.

The characteristic feature of altermagnets is a momentum-dependent band structure for each spin [1–3,15,16]. Indeed, momentum dependent band structures are observed by Angle-Resolved Photo-Emission Spectroscopy (ARPES) [17–21]. Furthermore, spin current is generated by applying electric field [22–25] owing to the above-mentioned characteristic band structure. However, there are only few works on topological properties [26] of altermagnets except for Majorana states [27–29].

In this paper, analyzing a bilayer system composed of an altermagnet and a two-dimensional topological insulator, we construct a topological phase diagram. It has intriguing features. On one hand, a topological phase transition occurs from a first-order topological insulator to a trivial insulator at a certain altermagnetization J_{cr} when the Néel vector is along the x or the y axis. This trivial insulator is intriguing since it is characterized by the emergence of edge states parallel to the Néel vector, which are as robust as topological edges. Furthermore, an edge state connects two valleys either in the occupied

band or in the unoccupied band, as is a reminiscence of the valley-protected edge states in the valley-Chern insulator [30]. Hence, we name it the x -axis crystalline valley-edge insulator (x -CVEI) or the y -axis crystalline valley-edge insulator (y -CVEI). On the other hand, the system becomes a second-order topological insulator (SOTI) when the Néel vector is along the z axis. We show that tunneling conductance has a sharp dependence on the Néel vector. In addition, the band gap has a dependence on the Néel vector, which is measured by optical absorption. Therefore, the Néel vector is experimentally determined by combining the tunneling conductance and the optical absorption spectra.

II. MODEL

We analyze the bilayer system where d -wave altermagnet is attached on a two-dimensional topological insulator. The Hamiltonian is given by

$$H = H_{\text{BHZ}} + H_{\text{Alter}}. \quad (1)$$

The topological insulator is described by the Bernevig-Hughes-Zhang (BHZ) model [31],

$$H_{\text{BHZ}} = M(k)\sigma_0 \otimes \tau_z + \lambda(\sin k_x \sigma_x \otimes \tau_x + \sin k_y \sigma_y \otimes \tau_x), \quad (2)$$

with $M(\mathbf{k}) = m - t(\cos k_x + \cos k_y)$, where m is the mass parameter, t is the hopping parameter, λ is the spin-orbit interaction, σ is the Pauli matrix for the spin, and τ is the Pauli matrix for the orbital. The BHZ model describes a topological insulator for $|m/(2t)| < 1$.

The effect of d -wave altermagnet is described by the Hamiltonian [1–3,27–29]

$$H_{\text{Alter}}(\mathbf{k}) = J(\cos k_x - \cos k_y)(\mathbf{s} \cdot \boldsymbol{\sigma}) \otimes \tau_x, \quad (3)$$

with $\mathbf{s} = (\sin \theta \cos \phi, \sin \theta \sin \phi, \cos \theta)$, where J is the magnitude of altermagnetization and $J\mathbf{s}$ is the Néel vector. The Néel vector is controlled by spin-orbit torque [32,33] or spin-split torque [34,35]. The characteristic feature of altermagnet is

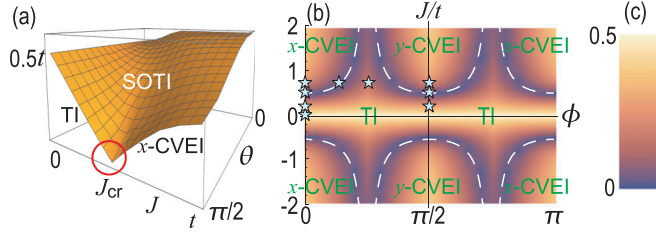


FIG. 1. (a) Bulk band gap in the (J, θ) plane with $0 \leq J \leq t$ and $\pi/2 \geq \theta \geq 0$, where we have set $\phi = 0$. The band gap closes at $J = J_{\text{cr}}$ and $\theta = \pi/2$. (b) Topological phase diagram in the $(\phi, J/t)$ plane with $0 \leq \phi \leq \pi$ and $-2 \leq J/t \leq 2$, where we have set $\theta = \pi/2$. The topological phase boundaries are analytically given by Eq. (7), which are illustrated by white dashed curves. A star represents a point at which the band structure in ribbon geometry is shown in Fig. 3. We have set $m = t$ and $\lambda = 0.5t$. (c) Color palette showing the band gap E/t for (b).

that the magnetization has a momentum dependence as in Hamiltonian (3).

III. BAND GAP

We study the bulk band gap. If the Néel vector is along the x axis, the energy spectrum is given by

$$E^2 = M^2(\mathbf{k}) + (\lambda \sin k_x + J(\cos k_x - \cos k_y))^2 + \lambda^2 \sin^2 k_y. \quad (4)$$

The minimum of the band gap is taken at $k_y = 0$. The solution $M(k_x, 0) = 0$ is given by $k_x = \pm \arccos(m/t - 1)$. The gap closing condition is

$$|J_{\text{cr}}/\lambda| = 1/\sqrt{2t/m - 1}. \quad (5)$$

We show the band gap in the J - θ plane at $\phi = 0$ in Fig. 1(a). The band gap closes at $J = J_{\text{cr}}$ when $\theta = \pi/2$.

If the Néel vector is in the x - y plane with angle ϕ , the energy spectrum is given by

$$E^2 = M^2(\mathbf{k}) + (\lambda \sin k_x + J \cos^2 \phi (\cos k_x - \cos k_y))^2 + (\lambda \sin k_y + J \sin^2 \phi (\cos k_x - \cos k_y))^2. \quad (6)$$

The bulk band gap closes at $J = J_{\text{cr}}$ with

$$\left| \frac{J_{\text{cr}}}{\lambda} \right| = \sqrt{\frac{m(2m + \sqrt{2}F) \sec^2 2\phi}{2(4t^2 - m^2)}}, \quad (7)$$

and $F \equiv \sqrt{4t^2 + m^2 + (4t^2 - m^2) \cos 4\phi}$. We have shown the gap-closing curves in Fig. 1(b). We later argue that they are topological phase boundaries when the Néel vector is within the x - y plane.

We show the band-gap structure in the m - J plane when the Néel vector is along the x axis is shown as a color plot in Fig. 2(a) and the gap-closing curves in Fig. 2(a). We later argue that they are topological phase boundaries. The trivial phase of the BHZ model remains as it is for $|m/(2t)| > 1$ and $J \neq 0$. However, a new type of trivial insulator emerge for $|m/(2t)| < 1$ and $J \neq 0$, as described below.

If the Néel vector is along the z axis ($\theta = 0$), the energy spectrum is given by

$$E^2 = M^2(\mathbf{k}) + \lambda^2 (\sin^2 k_x + \sin^2 k_y) + J^2 (\cos k_x - \cos k_y)^2. \quad (8)$$

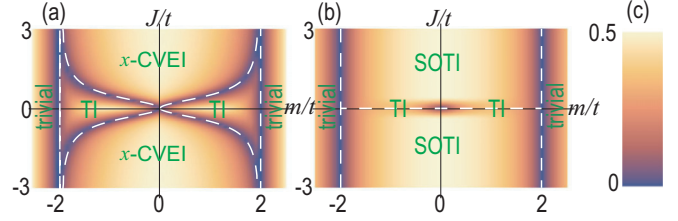


FIG. 2. (a) Topological phase diagram in the $(m/t, J/t)$ plane, where the Néel vector is along the x axis. The phase boundaries are analytically given by Eq. (5), which are illustrated by white dashed curves. (b) Topological phase diagram in the m - J plane, where the Néel vector is along the z axis. (c) Color palette showing the band gap E/t for (a) and (b).

The band gap is shown as a color plot in Fig. 2(b). It implies that the altermagnetization does not contribute to the gap closing and the gap closing condition is identical to that of the BHZ model, i.e., $m = \pm 2t$ as in Fig. 2(b). Hence, the topological phase boundaries remain the same as those of the BHZ model. However, the topological phase is changed from the first-order one to the second-order one, as described below.

IV. RIBBON GEOMETRY

We analyze the energy spectrum of the total Hamiltonian with ribbon geometry to see the topological property. In the absence of the altermagnetization, $J = 0$, there are topological edge states of the BHZ model (2), which cross at the momentum $k_x = 0$, as in Fig. 3(a).

If the altermagnetization is along the x axis, $J\mathbf{s}_x = (J, 0, 0)$, the crossing point of the topological edge states moves away from $k_x = 0$ for $J < J_{\text{cr}}$ as in Fig. 3(b1). At the critical point $J = J_{\text{cr}}$, the bulk band gap closes and the system is a semimetal as in Fig. 3(b2). For $J > J_{\text{cr}}$, each edge state connects either the occupied band or the unoccupied band, as in Fig. 3(b3). It indicates the system is trivial. Although the edge states are nontopological, they are robust against the order of the band gap because the turning point of the edge state much exceeds the band gap. Indeed, it requires perturbation much larger than the band gap to remove the trivial edge states. These nontopological edge states are as robust as topological edges. They are a reminiscence of the valley-protected edge states with each edge connecting two valleys either in the occupied band or in the unoccupied band [30]. We explicitly study the robustness against disorder later.

If the altermagnetization is along the y axis, $J\mathbf{s}_y = (0, J, 0)$, the topological edge states are maintained for $J < J_{\text{cr}}$ as in Fig. 3(c1). At the critical point $J = J_{\text{cr}}$, the bulk band gap closes as in Fig. 3(c2). Edge states disappear for $J > J_{\text{cr}}$ as in Fig. 3(c3).

We show the band structure when the altermagnetization is given by $J\mathbf{s} = J(\cos \phi, \sin \phi, 0)$ for the cases $\phi = \pi/8, \pi/4$ in Figs. 3(b4) and 3(c4), respectively. The bulk band gap closes in the vicinity of $\phi = \pi/8$ as in Figs. 3(b4) and 1(b). The valley-protected edge states become the topological edge states as in Figs. 3(c4) and 1(b).

If the altermagnetization is along the z axis, $J\mathbf{s}_z = (0, 0, J)$, the topological edge states anticross and a finite gap emerges in edge states as in Fig. 3(d). It means that the system is

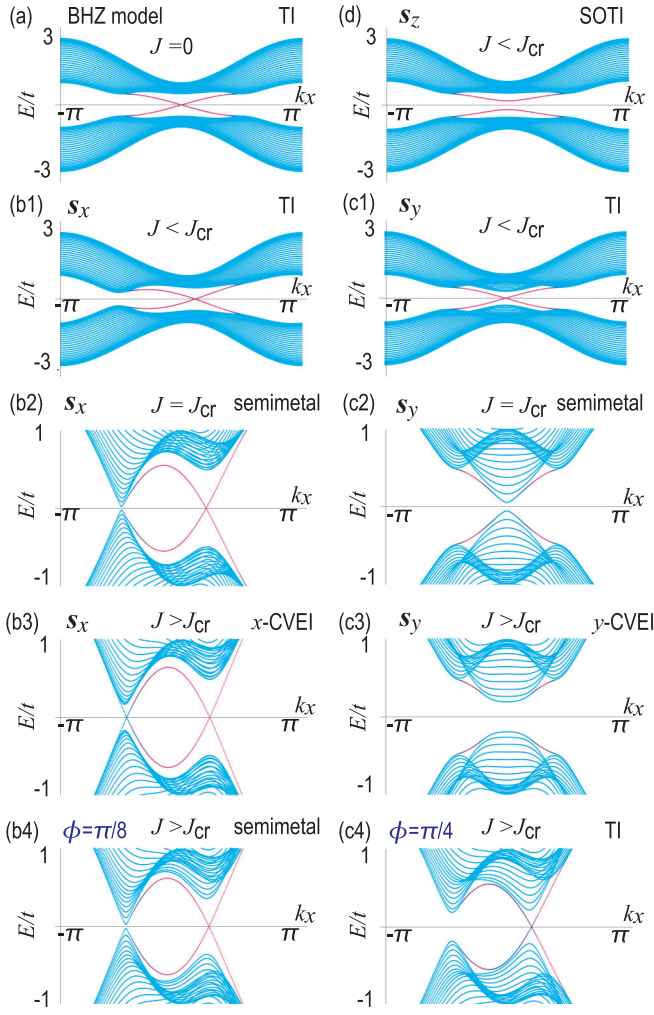


FIG. 3. Band structure in ribbon geometry for (a) no altermagnetization, [(b1)–(b3)] the Néel vector along the x axis, [(c1)–(c3)] the Néel vector along the y axis, (b4) the Néel vector with angle $\phi = \pi/8$, (c4) the Néel vector with angle $\phi = \pi/4$, and (d) the Néel vector along the z axis. The ribbon is taken along the x axis. The horizontal axis is the momentum k_x . (b1) and (c1) $J = 0.2t$. [(b2) and (c2)] $J = 0.5t = J_{cr}$. [(b3), (c3), (b4), and (c4)] $J = 0.7t$. We have set $m/t = 1$, $\lambda/t = 0.5$. Red color indicates the edge state, while cyan color indicates the bulk state. The point (ϕ, J) of each figure except (d) is indicated as a star in the phase diagram Fig. 1(b).

not a first-order topological insulator. We will soon see that the system is a second-order topological insulator, which is characterized by the emergence of corner states in square geometry.

V. SQUARE GEOMETRY

We investigate the energy spectrum of the total Hamiltonian with square geometry to see the topological property more in detail.

In the case of $Js_x = (J, 0, 0)$ or $Js_y = (0, J, 0)$, the edge states emerge along the x axis or the y axis, as in Fig. 4(a1) or 4(a2), respectively. Correspondingly, the energy spectrum is linear as a function of the eigenindex in the vicinity of the

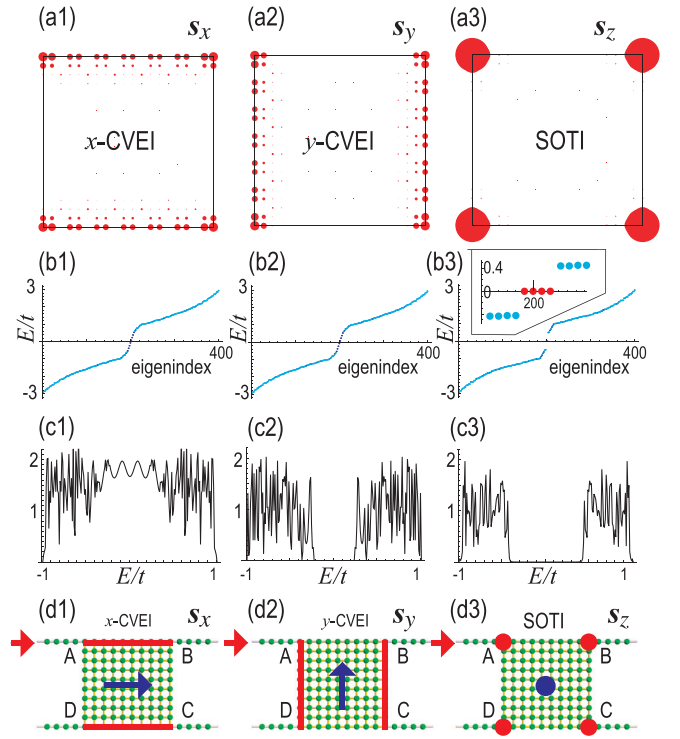


FIG. 4. [(a1)–(a3)] Spatial distribution of the zero-energy states marked in red. [(b1)–(b3)] Energy spectrum as a function of the eigenindex of the Hamiltonian. The inset in (b3) shows the presence of the four corner states at zero energy. [(c1)–(c3)] Tunneling conductance as a function of the energy. [(d1)–(d3)] Illustration of a square sample with four leads. [(a1)–(d1)] The Néel vector is along the x axis. [(a2)–(d2)] The Néel vector is along the y axis. [(a3)–(d3)] The Néel vector is along the z axis. We have set $m/t = 1$, $\lambda/t = 0.5$, and $J = 0.7t > J_{cr}$. Conductance between the leads A and B is calculated, where current is injected from the lead A as depicted by a red arrow.

zero energy, as in Fig. 4(b1) or 4(b2). These edge states are nontopological as we have argued in ribbon geometry. On the other hand, there are no edge states along the y axis or the x axis in the case of $Js_x = (J, 0, 0)$ or $Js_y = (0, J, 0)$ as in Fig. 4(a1) or 4(a2), respectively. It is a reminiscence of edge states of topological crystalline insulator [36]. The system is the x -axis crystalline valley-edge insulator (x -CVEI) in Fig. 4(a1) and the y -axis crystalline valley-edge insulator (y -CVEI) in Fig. 4(a2).

In the case of $Js_z = (0, 0, J)$, four topological corner states emerge as in Fig. 4(a3). Correspondingly, there are four zero-energy corner states within a finite gap as in Fig. 4(b3). As a result, the system is a second-order topological insulator.

VI. CONDUCTANCE

We show that the Néel vector is detectable by measuring the conductance in the setup shown in Figs. 4(d1)–4(d3), where four leads are attached to the corners of the square sample. We assume that the leads are single-atomic chains with semi-infinite length.

The conductance between two leads is calculated based on the Landauer formalism [37–41]. The conductance $\sigma(E)$ at

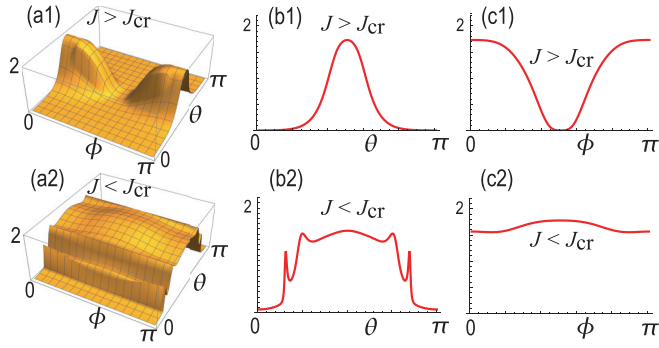


FIG. 5. [(a1) and (a2)] Tunneling conductance in the (ϕ, θ) plane. [(b1) and (b2)] Tunneling conductance as a function of θ at $\phi = 0$. The horizontal axis is $0 \leq \theta \leq \pi$. [(c1) and (c2)] Tunneling conductance as a function of ϕ at $\theta = \pi/2$. The horizontal axis is $0 \leq \phi \leq \pi$. [(a1)–(c1)] $J = 0.7t > J_{cr}$. [(a2)–(c2)] $J = 0.2t < J_{cr}$.

energy E is calculated as [37]

$$\sigma(E) = (e^2/h) \text{Tr}[\Gamma_L(E)G_D^\dagger(E)\Gamma_R(E)G_D(E)], \quad (9)$$

where $\Gamma_{R(L)}(E) = i[\Sigma_{R(L)}(E) - \Sigma_{R(L)}^\dagger(E)]$ is the line width with the self-energies $\Sigma_L(E)$ and $\Sigma_R(E)$ for the left and right leads, and $G_D(E) = [E - H - \Sigma_L(E) - \Sigma_R(E)]^{-1}$ is the Green function with the Hamiltonian H for the sample. The self energy of a single-atomic semi-infinite chain is analytically obtained [37] as $\Sigma_L(E) = \Sigma_R(E) = E - i\sqrt{|t^2 - E^2|}$.

First, we study the case $J > J_{cr}$. We show the conductance as a function of the energy E in Figs. 4(c1), 4(c2), and 4(c3). We have calculated the conductance between the leads A and B. The conductance is nonzero at $E = 0$ when the Néel vector is along the x axis as in Fig. 4(c1). It is understood that the current flows through the edge state along the x axis as in Fig. 4(d1). On the other hand, it is zero at $E = 0$ when the Néel vector is along the y axis as in Fig. 4(c2). It is because there is no edge state to carry the current along the x axis as in Fig. 4(d2). The conductance is also zero at $E = 0$ when the Néel vector is along the z axis as in Fig. 4(c3). It is because there is no edge state although corner states exist as in Fig. 4(d3). It seems to be difficult to differentiate the cases where the Néel vector is along the y axis or the z axis by measuring the conductance because the tunneling conductance is zero for both cases. However, it is differentiated by measuring the tunneling conductance between the leads A and D, where the conductance is nonzero if the Néel vector is along the y axis but zero if the Néel vector is along the z axis.

The conductance in the ϕ - θ plane is shown in Fig. 5(a1). The conductance as a function of θ at $\phi = 0$ is shown in Fig. 5(b1). The conductance takes the maximum value at $\theta = \pi/2$ and takes the minimum value at $\theta = 0$. The conductance as a function of ϕ at $\theta = \pi/2$ is shown in Fig. 5(c1). The conductance takes the maximum value at $\phi = 0$ and the minimum value at $\phi = \pi/2$. Hence, we can detect the Néel vector by measuring the conductance.

Next, we study the case $J < J_{cr}$. We show the conductance in the ϕ - θ plane in Fig. 5(a2). The dependence on the angle ϕ is tiny comparing with the case $J > J_{cr}$, as in Fig. 5(c2). It is because the system is a first-order topological insulator, where the topological edge state surround the sample. The

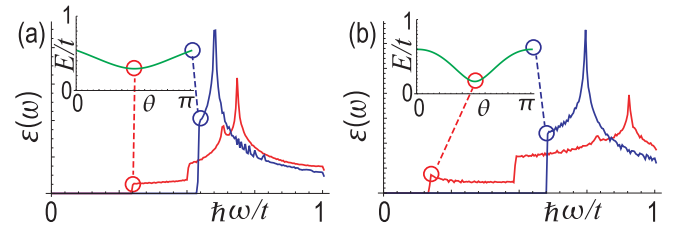


FIG. 6. Optical absorption spectra. Red curves indicate the spectra with $\theta = \pi/2$, while blue curves indicate that with $\theta = 0$. We have set $\phi = 0$. The horizontal axis is the photon energy $\hbar\omega$. Insets show the bulk band gap as a function of θ at $\phi = 0$. (a) $J = 0.2t < J_{cr}$ and (b) $J = 0.7t > J_{cr}$. The red and blue circles correspond to the optical absorption colored in red and blue.

conductance is zero for $\theta = 0$ and π as in the case of the system $J > J_{cr}$, as in Fig. 5(b2). It is because there are topological corner states but there are no edge states.

VII. OPTICAL ABSORPTION

We show that the band gap is observed by examining the optical absorption spectrum. We analyze the optical interband transition from the state $|u_v(\mathbf{k})\rangle$ in the valence band to the state $|u_c(\mathbf{k})\rangle$ in the conduction band. We apply a circularly polarized light, where the electromagnetic potential is given by $A(t) = (A_x \sin \omega t, A_y \cos \omega t)$.

The optical absorption is calculated based on the Kubo formula [36,42–45],

$$\varepsilon(\omega) = \frac{\pi e^2}{\varepsilon_0 m_c^2 \omega^2} \sum_i \int_{BZ} \frac{d\mathbf{k}}{(2\pi)^2} f(\mathbf{k}) |P_j(\mathbf{k})|^2 \times \delta[E_c(\mathbf{k}) - E_v(\mathbf{k}) - \hbar\omega], \quad (10)$$

where $P_j(\mathbf{k})$ is the optical matrix element $P_j(\mathbf{k}) \equiv m_0 \langle u_c(\mathbf{k}) | \frac{\partial H}{\partial k_j} | u_v(\mathbf{k}) \rangle$, $E_c(\mathbf{k})$ and $E_v(\mathbf{k})$ are the energies of the conduction and valence bands, and $f(\mathbf{k})$ is the Fermi distribution function.

We show the optical absorption spectra at $\theta = 0$ and $\pi/2$ in Fig. 6. There is a gap in the spectrum, implying the sudden occurrence of the optical absorption at the moment that the photon energy becomes the same as the band-gap energy. Hence, the band gap is measured by optical absorption experiments.

VIII. DISORDER EFFECTS

We study disorder effects. We introduce randomness distributing from $-\delta$ to δ by making the procedure $t \mapsto t(1 + \eta\delta)$, $m \mapsto m(1 + \eta\delta)$, $\lambda \mapsto \lambda(1 + \eta\delta)$, $J \mapsto J(1 + \eta\delta)$, where η is a random variable ranging from -1 to 1 . The band structures in nanoribbon geometry are shown in Fig. 7. The

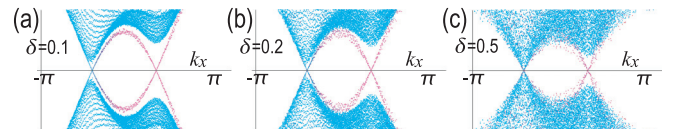


FIG. 7. Band structure in nanoribbon geometry in the presence of disorder with the strength (a) $\delta = 0.1$, (b) 0.2 , and (c) 0.5 .

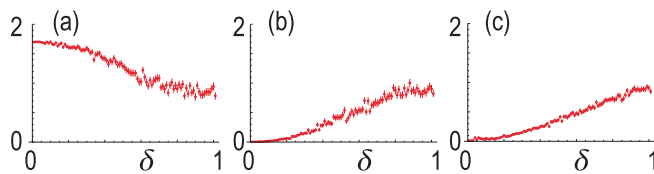


FIG. 8. The disorder effect on the conductance. (a) The Néel vector is along the x axis. (b) The Néel vector is along the y axis. (c) The Néel vector is along the z axis. The horizontal axis is the disorder δ . Average is taken 100 times.

edge states are robust for $\delta \lesssim 0.3$. The band gap at the left valley closes around $\delta \sim 0.3$. At the same time, the difference between the edge states and the bulk states become obscured in the vicinity of $k = 0$. Clear edge states survive at the right valley even for $\delta \sim 0.3$, which is obscured around $\delta \sim 0.7$. Hence, the valley edge states are as robust as topological edge states.

Next, we study a conductance at $E = 0$ corresponding to Fig. 4(c1) in the presence of disorders, which is shown in Fig. 8. First, we study the case where the Néel vector is along the x axis, whose result is shown in Fig. 8(a). The conductance

is robust for $\delta \lesssim 0.3$ corresponding to the robustness of the edge states in Fig. 7. The reduction of the conductance is less than one half even for $\delta = 1$. It means that the conductance measurement based on the valley edge states is very robust against disorders as well as topological edge states. Next, we study the case where the Néel vector is along the y and z axis, whose result is shown in Figs. 8(b) and 8(c), respectively. The conductance is zero in the absence of disorders. It gradually increases as the increase of disorder δ . The conductance between Figs. 8(a) and 8(b) is well differentiated for $\delta \lesssim 0.3$.

Note added. Recently, we became aware of a relevant paper [46]. Based on the density-functional theory, the system made of MnF_2 and bismuthene is shown to become a second-order topological insulator, where MnF_2 is an altermagnet, while bismuthene is a two-dimensional topological insulator.

ACKNOWLEDGMENTS

The author is very much grateful to S. Seki for helpful discussions on the subject. This work is supported by CREST, JST (Grant No. JPMJCR20T2) and Grants-in-Aid for Scientific Research from MEXT KAKENHI (Grant No. 23H00171).

- [1] L. Šmejkal, A. H. MacDonald, J. Sinova, S. Nakatsuji, and T. Jungwirth, Anomalous Hall antiferromagnets, *Nat. Rev. Mater.* **7**, 482 (2022).
- [2] L. Šmejkal, J. Sinova, and T. Jungwirth, Beyond conventional ferromagnetism and antiferromagnetism: A phase with nonrelativistic spin and crystal rotation symmetry, *Phys. Rev. X* **12**, 031042 (2022).
- [3] L. Šmejkal, J. Sinova, and T. Jungwirth, Emerging research landscape of altermagnetism, *Phys. Rev. X* **12**, 040501 (2022).
- [4] T. Jungwirth, X. Marti, P. Wadley, and J. Wunderlich, Antiferromagnetic spintronics, *Nat. Nanotechnol.* **11**, 231 (2016).
- [5] V. Baltz, A. Manchon, M. Tsoi, T. Moriyama, T. Ono, and Y. Tserkovnyak, Antiferromagnetic spintronics, *Rev. Mod. Phys.* **90**, 015005 (2018).
- [6] J. Han, R. Cheng, L. Liu, H. Ohno, and S. Fukami, Coherent antiferromagnetic spintronics, *Nat. Mater.* **22**, 684 (2023).
- [7] Z. Ni, A. V. Haglund, H. Wang, B. Xu, C. Bernhard, D. G. Mandrus, X. Qian, E. J. Mele, C. L. Kane, and L. Wu, Imaging the Néel vector switching in the monolayer antiferromagnet MnPSe_3 with strain-controlled Ising order, *Nat. Nanotechnol.* **16**, 782 (2021).
- [8] J. Godinho, H. Reichlov, D. Kriegner, V. Novak, K. Olejnik, Z. Kašpar, Z. Šoban, P. Wadley, R. P. Campion, R. M. Otxoa, P. E. Roy, J. Železný, T. Jungwirth, and J. Wunderlich, Electrically induced and detected Néel vector reversal in a collinear antiferromagnet, *Nat. Commun.* **9**, 4686 (2018).
- [9] K. Kimura, Y. Otake, and T. Kimura, Visualizing rotation and reversal of the Néel vector through antiferromagnetic trichroism, *Nat. Commun.* **13**, 697 (2022).
- [10] Y.-H. Zhang, T.-C. Chuang, D. Qu, and S.-Y. Huang, Detection and manipulation of the antiferromagnetic Néel vector in Cr_2O_3 , *Phys. Rev. B* **105**, 094442 (2022).
- [11] A. Fakhredine, R. M. Sattigeri, G. Cuono, and C. Autieri, Interplay between altermagnetism and nonsymmorphic symmetries generating large anomalous Hall conductivity by semi-Dirac points induced anticrossings, *Phys. Rev. B* **108**, 115138 (2023).
- [12] T. Tschirner, P. Keßler, R. D. G. Betancourt, T. Kotte, D. Kriegner, B. Buechner, J. Dufouleur, M. Kamp, V. Jovic, L. Šmejkal, J. Sinova, R. Claessen, T. Jungwirth, S. Moser, H. Reichlova, and L. Veyrat, Saturation of the anomalous Hall effect at high magnetic fields in altermagnetic RuO_2 , *APL Mater.* **11**, 101103 (2023).
- [13] T. Sato, S. Haddad, I. C. Fulga, F. F. Assaad, and J. van den Brink, Altermagnetic anomalous Hall effect emerging from electronic correlations, *arXiv:2312.16290*.
- [14] M. Leiviskä, J. Rial, A. Badura, R. L. Seeger, I. Kounta, S. Beckert, D. Kriegner, I. Joumard, E. Schmoranzarov, J. Sinova, O. Gomonay, A. Thomas, S. T. B. Goennenwein, H. Reichlová, L. Šmejkal, L. Michez, T. Jungwirth, and V. Baltz, Anisotropy of the anomalous Hall effect in the altermagnet candidate Mn_5Si_3 films, *arXiv:2401.02275*.
- [15] K.-H. Ahn, A. Hariki, K.-W. Lee, and J. Kunes, Antiferromagnetism in RuO_2 as d -wave Pomeranchuk instability, *Phys. Rev. B* **99**, 184432 (2019).
- [16] S. Hayami, Y. Yanagi, and H. Kusunose, Momentum-dependent spin splitting by collinear antiferromagnetic ordering, *J. Phys. Soc. Jpn.* **88**, 123702 (2019).
- [17] J. Krempaský, L. Šmejkal, S. W. D'Souza, M. Hajlaoui, G. Springholz, K. Uhlov, F. Alarab, P. C. Constantinou, V. Strocov, D. Usanov, W. R. Pudelko, R. Gonzalez-Hernandez, A. Birk Hellenes, Z. Jansa, H. Reichlov Z. Šob, R. D. Gonzalez Betancourt, P. Wadley, J. Sinova, D. Kriegner, J. Min, J. H. Dil and T. Jungwirth, Altermagnetic lifting of Kramers spin degeneracy, *Nature (London)* **626**, 517 (2024).

- [18] S. Lee, S. Lee, S. Jung, J. Jung, D. Kim, Y. Lee, B. Seok, J. Kim, B. G. Park, L. Šmejkal, C.-J. Kang, and C. Kim, Broken Kramers degeneracy in altermagnetic MnTe, *Phys. Rev. Lett.* **132**, 036702 (2024).
- [19] O. Fedchenko, J. Minar, A. Akashdeep, S. W. D'Souza, D. Vasilyev, O. Tkach, L. Odenbreit, Q. L. Nguyen, D. Kutnyakhov, N. Wind, L. Wenthous, M. Scholz, K. Rossnagel, M. Hoesch, M. Aeschlimann, B. Stadtmueller, M. Klauui, G. Schoenhense, G. Jakob, T. Jungwirth *et al.*, Observation of time-reversal symmetry breaking in the band structure of altermagnetic RuO₂, *Sci. Adv.* **10**, eadj4883 (2024).
- [20] T. Osumi, S. Souma, T. Aoyama, K. Yamauchi, A. Honma, K. Nakayama, T. Takahashi, K. Ohgushi, and T. Sato, Observation of a giant band splitting in altermagnetic MnTe, *Phys. Rev. B* **109**, 115102 (2024).
- [21] Z. Lin, D. Chen, W. Lu, X. Liang, S. Feng, K. Yamagami, J. Osiecki, M. Leandersson, B. Thiagarajan, J. Liu, C. Felser, and J. Ma, Observation of giant spin splitting and *d*-wave spin texture in room temperature altermagnet RuO₂, [arXiv:2402.04995](https://arxiv.org/abs/2402.04995).
- [22] M. Naka, S. Hayami, H. Kusunose, Y. Yanagi, Y. Motome, and H. Seo, Spin current generation in organic antiferromagnets, *Nat. Commun.* **10**, 4305 (2019).
- [23] R. Gonzalez-Hernandez, L. Šmejkal, K. Vborn, Y. Yahagi, J. Sinova, T. Jungwirth, and J. Železn, Efficient electrical spin splitter based on nonrelativistic collinear antiferromagnetism, *Phys. Rev. Lett.* **126**, 127701 (2021).
- [24] M. Naka, Y. Motome, and H. Seo, Perovskite as a spin current generator, *Phys. Rev. B* **103**, 125114 (2021).
- [25] A. Bose, N. J. Schreiber, R. Jain, D.-F. Shao, H. P. Nair, J. Sun, X. S. Zhang, D. A. Muller, E. Y. Tsymlal, D. G. Schlom, and D. C. Ralph, Tilted spin current generated by the collinear antiferromagnet ruthenium dioxide, *Nat. Electron.* **5**, 267 (2022).
- [26] R. M. Fernandes, V. S. de Carvalho, T. Birol, and R. G. Pereira, Topological transition from nodal to nodeless Zeeman splitting in altermagnets, *Phys. Rev. B* **109**, 024404 (2024).
- [27] D. Zhu, Z.-Y. Zhuang, Z. Wu, and Z. Yan, Topological superconductivity in two-dimensional altermagnetic metals, *Phys. Rev. B* **108**, 184505 (2023).
- [28] Y.-X. Li and C.-C. Liu, Majorana corner modes and tunable patterns in an altermagnet heterostructure, *Phys. Rev. B* **108**, 205410 (2023).
- [29] S. A. A. Ghorashi, T. L. Hughes, and J. Cano, Altermagnetic routes to Majorana modes in zero net magnetization, [arXiv:2306.09413](https://arxiv.org/abs/2306.09413).
- [30] M. Ezawa, Topological Kirchhoff law and bulk-edge correspondence for valley Chern and spin-valley Chern numbers, *Phys. Rev. B* **88**, 161406(R) (2013).
- [31] B. Andrei Bernevig, T. L. Hughes, S.-C. Zhang, Quantum spin Hall effect and topological phase transition in HgTe quantum wells, *Science* **314**, 1757 (2006).
- [32] H. Bai, Y. C. Zhang, Y. J. Zhou, P. Chen, C. H. Wan, L. Han, W. X. Zhu, S. X. Liang, Y. C. Su, X. F. Han, F. Pan, and C. Song, Efficient spin-to-charge conversion via altermagnetic spin splitting effect in antiferromagnet RuO₂, *Phys. Rev. Lett.* **130**, 216701 (2023).
- [33] L. Han, X. Fu, R. Peng, X. Cheng, J. Dai, L. Liu, Y. Li, Y. Zhang, W. Zhu, H. Bai, Y. Zhou, S. Liang, C. Chen, Q. Wang, X. Chen, L. Yang, Y. Zhang, C. Song, J. Liu, and F. Pan, Electrical 180° switching of Néel vector in spin-splitting antiferromagnet, *Sci. Adv.* **10**, eadn0479 (2024).
- [34] S. Karube, T. Tanaka, D. Sugawara, N. Kadoguchi, M. Kohda, and J. Nitta, Observation of spin-splitter torque in collinear antiferromagnetic RuO, *Phys. Rev. Lett.* **129**, 137201 (2022).
- [35] H. Bai, L. Han, X. Y. Feng, Y. J. Zhou, R. X. Su, Q. Wang, L. Y. Liao, W. X. Zhu, X. Z. Chen, F. Pan, X. L. Fan, and C. Song, Observation of spin splitting torque in a collinear antiferromagnet RuO, *Phys. Rev. Lett.* **128**, 197202 (2022).
- [36] M. Ezawa, Valleytronics in the surface of topological crystalline insulator: Elliptic dichroism and valley-selective optical pumping, *Phys. Rev. B* **89**, 195413 (2014).
- [37] S. Datta, *Electronic Transport in Mesoscopic Systems* (Cambridge University Press, Cambridge, England, 1995); *Quantum Transport: Atom to Transistor* (Cambridge University Press, England, 2005).
- [38] F. Muñoz-Rojas, D. Jacob, J. Fernández-Rossier, and J. J. Palacios, Coherent transport in graphene nanoconstrictions, *Phys. Rev. B* **74**, 195417 (2006).
- [39] L. P. Zârbo and B. K. Nikolić, Spatial distribution of local currents of massless Dirac fermions in quantum transport through graphene nanoribbons, *Europhys. Lett.* **80**, 47001 (2007); D. A. Areshkin and B. K. Nikolić, I-V curve signatures of nonequilibrium-driven band gap collapse in magnetically ordered zigzag graphene nanoribbon two-terminal devices, *Phys. Rev. B* **79**, 205430 (2009).
- [40] T. C. Li and S.-P. Lu, Quantum conductance of graphene nanoribbons with edge defects, *Phys. Rev. B* **77**, 085408 (2008).
- [41] M. Ezawa, Topological switch between second-order topological insulators and topological crystalline insulators, *Phys. Rev. Lett.* **121**, 116801 (2018).
- [42] W. Yao, D. Xiao, and Q. Niu, Valley-dependent optoelectronics from inversion symmetry breaking, *Phys. Rev. B* **77**, 235406 (2008).
- [43] D. Xiao, G.-B. Liu, W. Feng, X. Xu, and W. Yao, Coupled spin and valley physics in monolayers of MoS₂ and other group-VI dichalcogenides, *Phys. Rev. Lett.* **108**, 196802 (2012).
- [44] X. Li, T. Cao, Q. Niu, J. Shi, and J. Feng, Coupling the valley degree of freedom to antiferromagnetic order, *Proc. Natl. Acad. Sci. USA* **110**, 3738 (2013).
- [45] M. Ezawa, Spin-valley optical selection rule and strong circular dichroism in silicene, *Phys. Rev. B* **86**, 161407(R) (2012).
- [46] Y.-X. Li, Y. Liu, and C.-C. Li, Creation and manipulation of higher-order topological states by altermagnets, *Phys. Rev. B* **109**, L201109 (2024).